

Impact of Valley Degeneracy on Thermoelectric Properties of Zigzag Graphene Nanoribbons with Staggered Sublattice Potentials and Transverse Electric Fields

David M T Kuo

*Department of Electrical Engineering and Department of Physics,
National Central University, Chungli, 32001 Taiwan, China*

(Dated: August 22, 2024)

This study investigates the band inversion of flat bands in zigzag graphene nanoribbons (ZGNRs) using a tight-binding model. The band inversion results from symmetry breaking in the transverse direction, achievable through deposition on specific substrates such as separated silicon carbide or hexagonal boron nitride sheets. Upon band inversion, ZGNRs exhibit electronic structures characterized by valley degeneracy and band gap properties, which can be modulated by transverse electric fields. To explore the impact of this level degeneracy on thermoelectric properties, we employ Green's function techniques to calculate thermoelectric quantities in ZGNR segments with staggered sublattice potentials and transverse electric fields. Two carrier transport scenarios are considered: the chemical potential is positioned above and below the highest occupied molecular orbital. We analyze thermionic-assisted transport (TAT) and direct ballistic transport (DBT). Level degeneracy enhances the electric power factors of ZGNRs by increasing electrical conductance, while the Seebeck coefficient remains robust in the TAT scenario. Conversely, in DBT, the enhancement of the power factor primarily stems from improvements in the Seebeck coefficient at elevated temperatures.

I. INTRODUCTION

Thermoelectric heat engines (TEHs) function as electrical generators when exposed to temperature differentials and can alternatively operate as coolers when electric currents are applied [1–6]. This dual capability makes TEHs a promising solution for addressing environmental concerns related to CO₂ emissions. High-quality thermoelectric materials exhibit electron crystal-like properties and act as phonon insulators [1–3], characterized by long electron mean free paths and short phonon mean free paths. Consequently, extensive research has focused on exploring the thermoelectric properties of low-dimensional systems [7–13]. Materials composed of low-dimensional structures such as quantum wells [7], quantum wires [8–10], and quantum dots [11] demonstrate significant enhancements in thermoelectric properties. These structures effectively increase phonon scattering rates at interfaces, thereby reducing phonon thermal conductance, while maintaining electron thermoelectric properties comparable to bulk materials [7–13].

The efficiency of thermoelectric materials is quantified by the figure of merit $ZT = S^2 G_e T / \kappa$, where S , G_e and T denote the Seebeck coefficient, electrical conductance, and equilibrium temperature, respectively. Thermal conductance κ comprises contributions from electron thermal conductance κ_e and phonon thermal conductance κ_{ph} . Initial theoretical work by Hicks and Dresselhaus, using the effective mass model, suggested that quasi-one-dimensional systems with diameters less than one nanometer could achieve $ZT = 14$ [14], sparking extensive research into the thermoelectric properties of various material quantum wires and those exhibiting one-dimensional topological states using first-principles methods [15–23].

The landmark discovery of graphene in 2004 by Novoselov and Geim [24] prompted investigations into

quasi-one-dimensional electronics, optoelectronics, and thermoelectric devices utilizing nanowires formed from two-dimensional materials [25,26]. Graphene nanoribbons (GNRs) have garnered attention due to their low thermal conductance, as reported in theoretical calculations [15], owing to their atomic-scale thickness. Edge-disordered zigzag GNRs (ZGNRs) [16], semiconducting armchair GNRs (AGNRs) [17], and GNRs with topological states [22] exhibit significantly enhanced ZT values compared to gapless graphenes [23]. These GNRs achieve ZT values greater than one, although their power factors are relatively small. TE devices require ZT values exceeding three, along with optimized electrical power outputs [27]. Enhancing the power factor values through increased level degeneracy has been a focal point of numerous studies [28–36]. Materials like *GeTe* exhibit very high ZT at elevated temperatures, where valley degeneracy may play a crucial role [32–36].

While bottom-up techniques provide precise atomic control over various GNRs, the existence of semiconducting GNRs with valley degeneracy has not yet been reported [37–55]. To investigate the impact of valley degeneracy on the thermoelectric properties of GNRs, we propose utilizing ZGNRs with staggered sublattice potentials. These potentials can be implemented by coupling the ZGNRs to substrates such as silicon carbide or hexagonal boron nitride [56]. We consider three configurations of ZGNRs with different staggered sublattice potentials denoted as (a) w-AB/n-C/w-AB, (b) w-AB/n-C/w-BA, and (c) w-BA/n-C/w-AB, where integers w and n represent the widths of ZGNRs with and without sublattice potential, respectively. The w-AB/4-C/w-AB structures exhibit semiconducting behavior and valley degeneracy in two valleys within the conduction and valence subbands. This valley degeneracy arises from band inversion of the flat bands induced by inversion symmetry breaking in the transverse direction, facilitated by the underlying

substrates. The primary objective of this study is to investigate how valley degeneracy affects the thermoelectric properties of ZGNRs supported on these substrates.

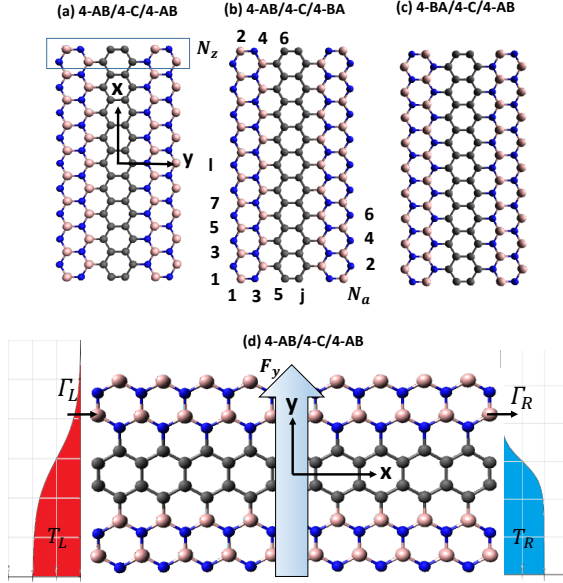


FIG. 1: Schematic diagram illustrating three types of ZGNRs with staggered sublattice potentials: (a) 4-AB/4-C/4-AB, (b) 4-AB/4-C/4-BA, and (c) 4-BA/4-C/4-AB. In (a), ZGNR without inversion symmetry in the y direction. The square bracket indicates the unit cell of 4-AB/4-C/4-AB. In (b) and (c), ZGNRs remain the inversion symmetry in the y direction. Atoms marked with blue and white colors indicate these carbon atoms on the boron nitride substrates. Diagram (d) depicts the armchair edges of the 4-AB/4-C/4-AB segment in contact with electrodes. Symbols Γ_L (Γ_R) represent the electron tunneling rate between the left (right) electrode and the leftmost (rightmost) atoms at the armchair edges, and T_L (T_R) denotes the equilibrium temperature of the left (right) electrode. F_y denotes a uniform transverse electric field along the armchair direction.

II. CALCULATION METHODOLOGY

To explore the thermoelectric properties of ZGNRs with sublattice potentials connected to the electrodes, we utilize a combination of the tight-binding model and the Green's function technique. The system Hamiltonian consists of two components: $H = H_0 + H_{ZGNR}$. Here, H_0 signifies the Hamiltonian of the electrodes, encompassing the interaction between the electrodes and the ZGNR. Meanwhile, H_{ZGNR} represents the Hamiltonian for the ZGNRs and can be expressed as follows:

$$H_{ZGNR} = \sum_{\ell,j} E_{\ell,j} d_{\ell,j}^\dagger d_{\ell,j} - \sum_{\ell,j} \sum_{\ell',j'} t_{(\ell,j),(\ell',j')} d_{\ell,j}^\dagger d_{\ell',j'} + h.c. \quad (1)$$

Here, $E_{\ell,j}$ represents the on-site energy of the orbital in the ℓ -th row and j -th column. The operators $d_{\ell,j}^\dagger$ and $d_{\ell,j}$ create and annihilate an electron at the atom site denoted by (ℓ,j) . The parameter $t_{(\ell,j),(\ell',j')}$ characterizes the electron hopping energy from site (ℓ',j') to site (ℓ,j) . We set $t_{(\ell,j),(\ell',j')} = t_{pp\pi} = 2.7$ eV for the nearest-neighbor hopping strength. Because we have considered ZGNRs on the hexagonal boron nitride substrates, staggered sublattice potentials are $E_A = \delta$ and $E_B = -\delta$, which are relative to p_z orbital of carbon atom $E_C = 0$ [57]. Note that if one stack ZGNRs on other two dimensional material substrates and then spin orbital coupling may not be ignored [58].

In the linear response region, the electrical conductance (G_e), Seebeck coefficient (S) and electron thermal conductance (κ_e) can be computed using $G_e = e^2 \mathcal{L}_0$, $S = -\mathcal{L}_1 / (eT \mathcal{L}_0)$ and $\kappa_e = \frac{1}{T} (\mathcal{L}_2 - \frac{\mathcal{L}_1^2}{\mathcal{L}_0})$ with \mathcal{L}_n ($n = 0, 1, 2$) defined as

$$\mathcal{L}_n = \frac{2}{h} \int d\varepsilon \mathcal{T}_{LR}(\varepsilon) (\varepsilon - \mu)^n \frac{\partial f(\varepsilon)}{\partial \mu}. \quad (2)$$

Here, $f(\varepsilon) = 1 / (1 + \exp((\varepsilon - \mu) / k_B T))$ represents the Fermi distribution function of electrodes at equilibrium chemical potential μ . The constants e , h , k_B , and T denote the electron charge, Planck's constant, Boltzmann's constant, and the equilibrium temperature of the electrodes, respectively. $\mathcal{T}_{LR}(\varepsilon)$ signifies the transmission coefficient of a ZGNR connected to electrodes, and it can be calculated using the formula $\mathcal{T}_{LR}(\varepsilon) = 4 \text{Tr}[\Gamma_L(\varepsilon) G^r(\varepsilon) \Gamma_R(\varepsilon) G^a(\varepsilon)]$ [30, 59], where $\Gamma_L(\varepsilon)$ and $\Gamma_R(\varepsilon)$ denote the tunneling rate (in energy units) at the left and right leads, respectively, and $G^r(\varepsilon)$ and $G^a(\varepsilon)$ are the retarded and advanced Green's functions of the GNRs, respectively. The tunneling rates ($\Gamma_{L(R)}(\varepsilon) = \text{Im} \sum_{L(R)}^r \Gamma(\varepsilon)$) are determined by the imaginary part of the self-energy originating from the coupling between the left (right) electrode and its adjacent GNR atoms. In terms of tight-binding orbitals, $\Gamma_\alpha(\varepsilon)$ and Green's functions are matrices. For simplicity, $\Gamma_\alpha(\varepsilon)$ for interface atoms possesses diagonal entries with a common value of Γ_t [30]. Contact properties between 2D nanostructures and metallic electrodes typically induce Schottky barriers [60–64], posing challenges in achieving tunable Fermi energy due to Fermi energy pinning [65]. Despite numerous theoretical studies striving to elucidate this crucial behavior from first principles, the theoretical limitations result in obtaining only qualitative results regarding Γ_t arising from the contact junction [52].

III. RESULTS AND DISCUSSION

A. Electronic Structures of ZGNRs with staggered sublattice potentials

To depict the electronic properties of ZGNRs with staggered sublattice potentials, as shown in Fig. 1(a)-1(c), we calculated the electronic structures of three configurations: 4-AB/4-C/4-AB, 4-BA/4-C/4-AB, and 4-AB/4-C/4-BA, based on the Hamiltonian in Eq. (1). These electronic structures are presented in Fig. 2(a), 2(b), and 2(c), respectively. Among ZGNRs with sublattice potentials, only the w-AB/4-C/w-AB structure exhibits a semiconducting phase. Notably, the w-AB/4-C/w-AB structure also displays valley degeneracy in the frontier conduction and valence subbands, albeit with shallow valley depths. In contrast, both the 4-BA/4-C/4-AB and 4-AB/4-C/4-BA configurations exhibit metallic phases, characterized by asymmetrical electronic structures distinct from those of ZGNRs without staggered sublattice potentials, where symmetrical flat bands are observed near the charge neutral point (CNP) [66,67].

Figures 2(d), 2(e), and 2(f) illustrate the electronic structures of w-AB/4-C/w-AB for three different widths, where $w = 8, 12$ and 16 . The valley structure of the frontier conduction and valence subbands is sensitive to the widths of ZGNRs coupled to the substrates. Based on the findings of Fig. 2, a semiconducting phase with valley degeneracy emerges from the w-AB/4-C/w-AB structure due to broken inversion symmetry in the transverse direction. However, this valley structure is suppressed by the coupling between the frontier and secondary conduction (valence) subbands. The mechanism of valley degeneracy in topological thermoelectric materials remains a topic of current interest [68-70].

When transverse electric fields F_y are applied to ZGNRs, the electric potential $U = eF_y y$ affects each site of the ZGNRs [71]. Here, $F_y = V_y/L_a$, where V_y is the applied bias and L_a is the width of the ZGNRs. We investigate the electronic structures of the 4-AB/4-C/4-AB structure under transverse electric fields, as depicted in Fig. 3. Increasing V_y results in a reduction of the band gap in the 4-AB/4-C/4-AB structure. At $V_y = 0.9$ V, the electronic structures of the frontier conduction and valence subbands exhibit flat bands. Conversely, negative values of V_y reveal more pronounced valley structures in Fig. 3(d), 3(e), and 3(f). This negative V_y enhances the inversion symmetry breaking of ZGNRs [70]. The directionality of the electric field influences the valley structure of 4-AB/4-C/4-AB ZGNRs with asymmetrical staggered sublattice potentials. Such an electric field-dependent valley structure could potentially find applications in valleytronics [72-75].

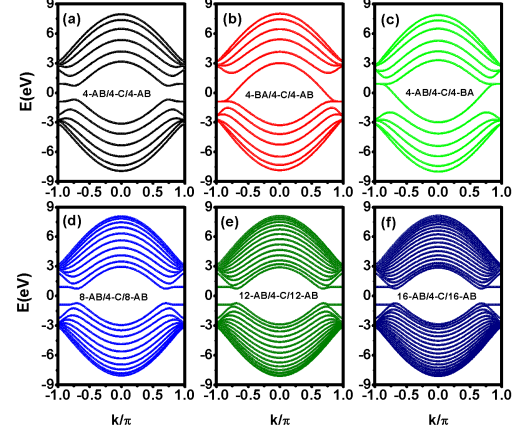


FIG. 2: Electronic structures of ZGNRs with various configurations: (a) 4-AB/4-C/4-AB, (b) 4-BA/4-C/4-AB, (c) 4-AB/4-C/4-BA, (d) 8-AB/4-C/8-AB, (e) 12-AB/4-C/12-AB, and (f) 16-AB/4-C/16-AB. Here, we have adopted $E_A = -E_B = \delta = 0.9$ eV.

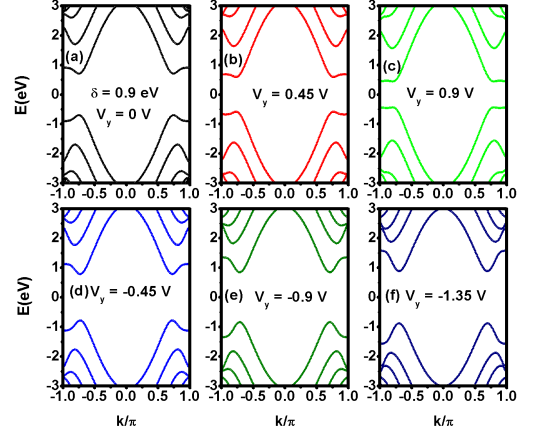


FIG. 3: Electronic structures of 4-AB/4-C/4-AB ZGNRs with staggered sublattice potential $\delta = 0.9$ eV for various transverse applied voltages: (a) $V_y = 0$ V, (b) $V_y = 0.45$ V, (c) $V_y = 0.9$ V, (d) $V_y = -0.45$ V, (e) $V_y = -0.9$ V and (f) $V_y = -1.35$ V.

B. Transmission Coefficient of 4-AB/4-C/4-AB under Transverse Electric Fields

Synthesizing ZGNRs longer than 20 nm using bottom-up techniques remains challenging [76, 77]. Therefore, investigating the size effect of ZGNR segments on valley degeneracy is crucial. Here, we present the energy levels of ZGNR segments with $N_z = 81$ ($L_z = 9.84$ nm) as functions of the sublattice potential magnitude δ under various transverse electric fields in Fig. 4. When $\delta = 0$ and

$V_y = 0$, metallic ZGNRs exhibit discrete energy levels due to their finite sizes, as seen in Fig. 4(a). The energy levels E_{HO} (highest occupied molecular orbital, HOMO) and E_{LU} (lowest unoccupied molecular orbital, LUMO) are very close to the charge neutral point ($E = 0$) due to small overlap between the wave functions of zigzag edge states. As δ increases, E_{HO} and E_{LU} separate. Moreover, the number of level degeneracies, indicated by a wider range of levels with stronger color intensity, increases for $\delta > 0.45$ eV. These results in Fig. 4(a) can be understood in the context of the electronic structures of 4-AB/4-C/4-AB ZGNRs shown in Appendix A (Fig. A.1). The extent of level degeneracy in 4-AB/4-C/4-AB ZGNR segments corresponds to the depth of valley structures in infinite 4-AB/4-C/4-AB ZGNRs. Upon applying transverse electric fields, the patterns of energy levels with respect to δ change dramatically, as illustrated in Figs. 4(b), 4(c), and 4(d). The range of energy level degeneracy with respect to transverse electric fields aligns with the electronic structures shown in Fig. 3. Notably, while ZGNRs without staggered sublattice potential have demonstrated valley structures under strong transverse electric fields, the extent of level degeneracy is limited, and the electric field-direction-dependent valley structure disappears [78]

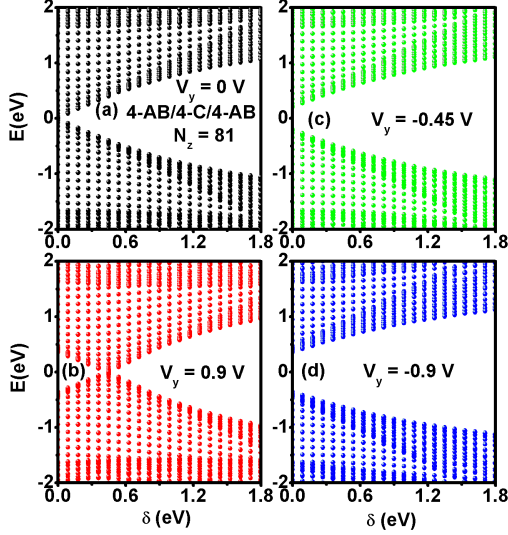


FIG. 4: Energy levels of 4-AB/4-C/4-AB ZGNR segments as functions of δ for various transverse applied voltages: (a) $V_y = 0$ V, (b) $V_y = 0.9$ V, (c) $V_y = -0.45$ V, and (d) $V_y = -0.9$ V. The ZGNR segment with length L_z is characterized by $L_z = 9.84$ nm ($N_z = 81$).

Since the transmission coefficient spectra of nanostructures are influenced by the wave-functions of their energy levels [30], understanding the wave functions of each energy level for 4-AB/4-C/4-AB ZGNR segments with various δ values is crucial. In Fig. 5(a), the probability densi-

ties $|\Psi(\ell, j)(E = 0)|^2$ demonstrate localized and symmetrical zigzag edge states in the y direction for $\delta = 0$ eV and $V_y = 0$. Figures 5(b) and 5(c) show the probability densities of $E_{HO} = -0.253$ eV and $E_{LU} = 0.253$ eV, respectively, depicting the wave functions of the HOMO and the LUMO at $\delta = 0.27$ eV. Analysis of their probability density distributions reveals that $E_{HO(LU)} = \mp 0.253$ eV are primarily determined by E_B and E_A , respectively. The maximum probability densities $|\Psi(\ell, j)(E_{HO})|^2$ and $|\Psi(\ell, j)(E_{LU})|^2$ are concentrated at $j = 12$ and $j = 1$, respectively, with $|\Psi(\ell, j)(E_{HO})|^2$ being vanishingly small for $j = 7, 9$ and 11 , and $|\Psi(\ell, j)(E_{LU})|^2$ for $j = 2, 4$ and 6 . In Fig. 5(d), 5(e) and 5(f) at $\delta = 0.9$ eV, we present the probability density distributions of $E_1 = -0.704$ eV, $E_2 = -0.7053$ eV and $E_3 = -0.7284$ eV, which are below the CNP. These states exhibit delocalized and asymmetrical characteristics in the y direction, indicative of band inversion in flat bands for ZGNRs. The probability densities $|\Psi(\ell = 1, j)(E_i)|^2$ and $|\Psi(\ell = 81, j)(E_i)|^2$ significantly influence the transmission coefficient spectra of 4-AB/4-C/4-AB ZGNR segments with armchair edges coupled to the electrodes shown in Fig. 1(d).

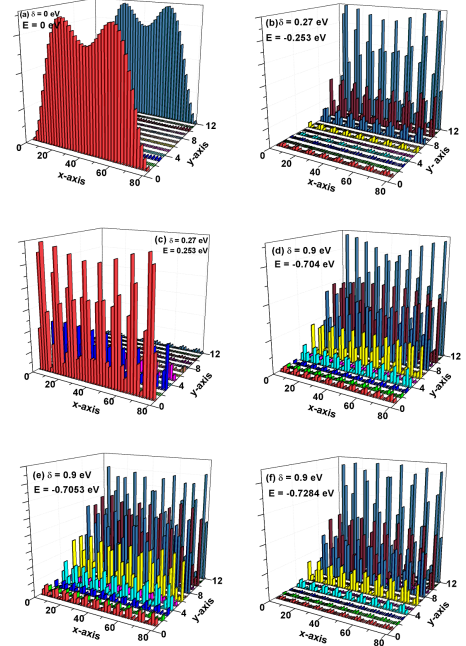


FIG. 5: Probability density of 4-AB/4-C/4-AB ZGNRs with different staggered sublattice potentials in the absence of V_y : (a) $\delta = 0$ and $E = 0$, (b) $\delta = 0.27$ eV and $E_{HO} = -0.253$ eV, (c) $\delta = 0.27$ eV and $E_{LU} = 0.253$ eV, (d) $\delta = 0.9$ eV and $E_1 = -0.704$ eV, (e) $\delta = 0.9$ eV and $E_2 = -0.7053$ eV, and (f) $\delta = 0.9$ eV and $E_3 = -0.7284$ eV.

According to Eq. (2), the thermoelectric quantities of ZGNRs, including electrical conductance, Seebeck coefficient, and electron thermal conductance, are deter-

mined by the area and shape of the transmission coefficient ($\mathcal{T}_{LR}(\varepsilon)$) curve. Therefore, it is necessary to clarify the effects of contact properties on $\mathcal{T}_{LR}(\varepsilon)$. In Fig. 6, we present the calculated $\mathcal{T}_{LR}(\varepsilon)$ curves of 4-AB/4-C/4-AB ZGNR segments for various Γ_t values, which depend on the contact geometries and the electrode materials. For simplicity of analysis, $\varepsilon \leq 0$ is considered throughout this article. As seen in Fig. 6(a), the $\mathcal{T}_{LR}(\varepsilon)$ curve shows many discrete peaks under a weak coupling strength of $\Gamma_t = 0.27$ eV. With increasing Γ_t values, the area of $\mathcal{T}_{LR}(\varepsilon)$ curve increases, and the shapes of these areas also change. For instance, in Fig. 6(b), the area of $\mathcal{T}_{LR}(\varepsilon)$ curve shows a right-triangle shape with a steep change with respect to ε on the side toward the central gap. In Figs. 6(c) and 6(d), the areas of $\mathcal{T}_{LR}(\varepsilon)$ curves show rectangular shapes. For $\Gamma_t = 2.7$ eV, we observe an arch shape in Fig. 6(f). The level degeneracy is characterized by $\mathcal{T}_{LR}(\varepsilon)$ with values near two. For $\Gamma_t = 2.7$ eV, the electrode materials can be regarded as graphenes since $\Gamma_t = t_{pp\pi}$.

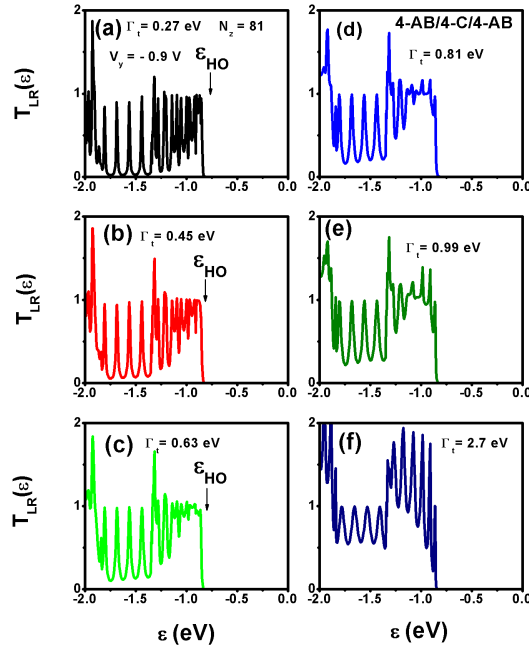


FIG. 6: Transmission coefficient $\mathcal{T}_{LR}(\varepsilon)$ of 4-AB/4-C/4-AB ZGNR segments as functions of ε for various Γ_t values at $N_a = 12$, $N_z = 81$, and $V_y = -0.9$ V: (a) $\Gamma_t = 0.27$ eV, (b) $\Gamma_t = 0.45$ eV, (c) $\Gamma_t = 0.63$ eV, (d) $\Gamma_t = 0.81$ eV, (e) $\Gamma_t = 0.99$ eV, and (f) $\Gamma_t = 2.7$ eV. Here, $N_z = 81$ corresponds to a channel length of $L_z = 9.84$ nm.

As observed in Fig. 3, the curvature of the conduction (valence) subband in 4-AB/4-C/4-AB ZGNRs can be adjusted by a transverse electric field. This indicates that the effective masses of electrons (holes) and the density of

states near the subband edge depend on the applied voltage strength (V_y). It is expected that the $\mathcal{T}_{LR}(\varepsilon)$ curves are also significantly influenced by these transverse electric fields. To examine the impact of V_y , we present the calculated $\mathcal{T}_{LR}(\varepsilon)$ curves for 4-AB/4-C/4-AB ZGNR segments across various V_y values in Fig. 7. The spectra of $\mathcal{T}_{LR}(\varepsilon)$ depend not only on the magnitude of the electric fields but also on their direction. Moreover, the shapes of the $\mathcal{T}_{LR}(\varepsilon)$ curves vary distinctly with each V_y . In reference [27], it was noted that efficient heat engines with optimized power outputs can be realized when the $\mathcal{T}_{LR}(\varepsilon)$ curve exhibits an ideal rectangular shape. However, such an ideal rectangular curve ($\mathcal{T}_{LR}(\varepsilon) = N_v$ for $\varepsilon < \varepsilon_{HO}$, where N_v represents valley degeneracy) exists only in infinitely long 1D systems without defects [60-64].

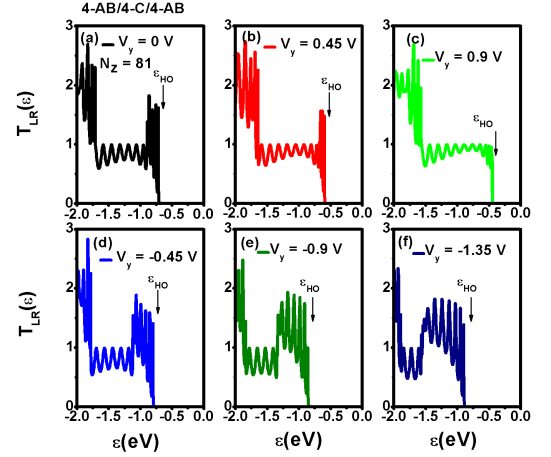


FIG. 7: Transmission coefficient $\mathcal{T}_{LR}(\varepsilon)$ of 4-AB/4-C/4-AB ZGNR segments as functions of ε for various V_y values at $\Gamma_t = 2.7$ eV. Panels show (a) $V_y = 0$ V, (b) $V_y = 0.45$ V, (c) $V_y = 0.9$ V, (d) $V_y = -0.45$ V, (e) $V_y = -0.9$ V, and (f) $V_y = -1.35$ V. Other physical parameters are identical to those in Fig. 6.

C. Thermoelectric Properties of Finite 4-AB/4-C/4-AB ZGNR Segments

The transmission coefficients presented in Fig. 6 and Fig. 7 reveal the electrical conductance $G_e(\mu)$ of 4-AB/4-C/4-AB ZGNR segments at zero temperature, given by $G_e(\mu) = G_0 \mathcal{T}_{LR}(\mu)$, where $G_0 = \frac{2e^2}{h}$ is the quantum conductance. For ZGNRs with two valley degeneracy, the ideal $G_e(\mu)$ reaches $\frac{4e^2}{h}$ [79]. To illustrate the contact effects on the thermoelectric properties of 4-AB/4-C/4-AB ZGNRs, we plot the curves of electrical conductance (G_e), Seebeck coefficient (S), power factor ($PF = S^2 G_e$), and figure of merit (ZT) at $T = 324$ K in Fig. 8. Throughout this article, we use specific constants: $G_0 = 2e^2/h = 77.5 \mu S$ for electrical conductance, $k_B/e = 86.25 \mu V/K$ for the Seebeck coefficient,

and $2k_B^2/h = 0.575pW/K^2$ for the power factor.

In Fig. 8(a), the curves of $G_e(\mu)$ at finite temperature are influenced by the averaged $\mathcal{T}_{LR}(\varepsilon)$ curves, with the averaging range of ε determined by $\frac{1}{4k_B T \cosh^2((\varepsilon - \mu)/(2k_B T))}$. At low temperatures, states near μ dominate charge transport. Fig. 8(b) shows that the maximum Seebeck coefficient occurs at small $\Gamma_t = 0.27$ eV, although the six S curves nearly coincide in the range $\varepsilon_{HO} < \mu < -0.45$ eV. In Fig. 8(c) and 8(d), the maximum power factor $PF_{max} = 1.16$ and figure of merit $ZT_{max} = 3.46$ are observed at $\Gamma_t = 0.81$ eV. The figure of merit ZT is calculated using $ZT = \frac{S^2 G_e T}{\kappa_e + \kappa_{ph}}$, where κ_{ph} represents the phonon thermal conductance of the 4-AB/4-C/4-AB structure, approximated here as $\kappa_{ph} = F_s \kappa_{GNR}$ with $\kappa_{GNR} = \frac{\pi^2 k_B^2 T}{3h}$. Here, $F_s = 0.1$ accounts for substrate effects, reducing κ_{ph} as shown theoretically for ZGNRs with boron nitride interfaces [80–83]. Note that PF_{max} and ZT_{max} for $\Gamma_t = 0.81$ eV occur at chemical potentials $\mu = -0.823$ eV and $\mu = -0.787$ eV, respectively. ZT values exceeding three are found only within a very small range of μ . The optimized chemical potential for maximizing the power factor is 21 meV above $\varepsilon_{HO} = -0.844$ eV, known as thermionic-assisted transport (TAT). Experimentally, achieving such optimized positions of electrode chemical potentials depicted in Fig. 8 presents a challenge due to difficulties in precise modulation[36]. Introducing transverse electric fields may offer practical means to adjust the separation between ε_{HO} and μ levels.

According to the results in Fig. 8, the thermoelectric performance at room temperature deteriorates when the chemical potential μ falls below ε_{HO} . This scenario, known as direct ballistic transport (DBT), corresponds to $\mu < \varepsilon_{HO}$. For an ideal scenario where $\mathcal{T}_{LR}(\varepsilon) = N_v$, the Seebeck coefficients approach zero at low temperatures when $\mu < \varepsilon_{HO}$ because S does not favor the transmission coefficient curve with symmetrical behavior around $\varepsilon \approx \mu$. This highlights the significant impact of the shape of the $\mathcal{T}_{LR}(\varepsilon)$ curve on enhancing S in DBT conditions.

Therefore, we analyze the $\mathcal{T}_{LR}(\varepsilon)$ curves at $V_y = -0.9$ V and $V_y = 0.9$ V shown in Fig. 7(e) and 7(c), respectively, and present their electrical conductance, Seebeck coefficient, and power factor as functions of temperature (T) for three values of chemical potential $\Delta = \mu - \varepsilon_{HO}$ in Fig. 9. Specifically, for $V_y = -0.9$ V, we consider $\Delta = -20$ meV, $\Delta = -29$ meV, and $\Delta = -38$ meV. For $V_y = 0.9$ V with $\varepsilon_{HO} = -0.4454$ eV, we consider $\Delta = -9$ meV, $\Delta = -18$ meV, and $\Delta = -27$ meV. In Fig. 9(a) and 9(d), the electrical conductances at low temperatures directly reflect the transmission coefficient spectra. As the temperature increases to and exceeds room temperature ($k_B T > 27$ meV), the electrical conductances become less sensitive to temperature variations.

Unlike electrical conductance, Seebeck coefficients exhibit a temperature-dependent bipolar behavior. The positive and negative signs reflect competition between electrons and holes, corresponding to occupied states

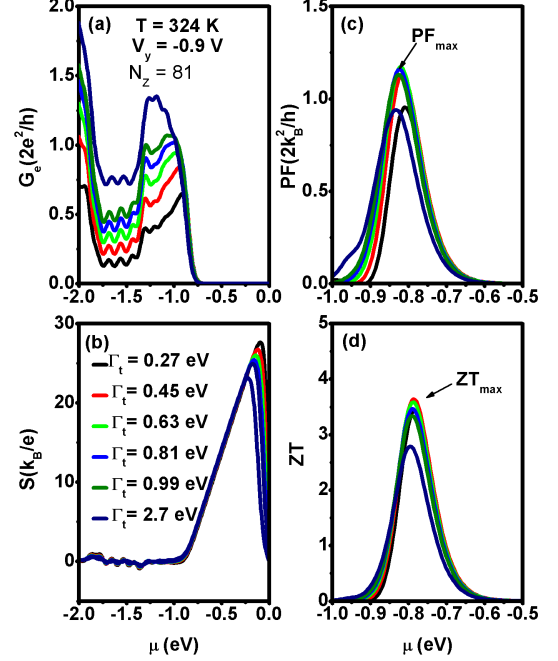


FIG. 8: (a) Electrical conductance G_e , (b) Seebeck coefficient (S), (c) power factor (PF), and (d) figure of merit (ZT) as functions of chemical potential μ for different Γ_t values at $T = 324$ K. Other physical parameters are identical to those in Fig. 6.

above μ and unoccupied states below μ , respectively. As temperature increases beyond $k_B T > 10$ meV, positive S values indicate dominance of hole carriers. In this temperature range, higher temperatures lead to larger Seebeck coefficients, highlighting temperature-dependent electron-hole asymmetry in DBT when μ approaches or falls below ε_{HO} . For instance, the curve with $\Delta = -20$ meV and $V_y = -0.9$ V exhibits a maximum S value of $138 \mu V/K$ at $k_B T = 80$ meV, which is higher than the $120 \mu V/K$ observed for $\Delta = -9$ meV and $V_y = 0.9$ V at the same temperature. Consequently, the maximum power factor $PF_{max} = 1.21 \cdot \frac{2k_B^2}{h}$ at $k_B T = 80$ meV occurs for $\Delta = -20$ meV and $V_y = -0.9$ V.

The variations in chemical potential depicted in Fig. 9 correspond to behaviors observed in codoped Germanium Telluride ($Ge_{1-x-y}Sb_xBi_yTe$) thermoelectric materials. It is noteworthy that the electronic structures of $GeTe$ exhibit multiple quasi-1D valley structures near the Fermi energy [36]. The behaviors of electrical conductance, Seebeck coefficient, and power factor with respect to temperature in Fig. 9(a), 9(b), and 9(c) effectively elucidate the thermoelectric properties of these materials within the temperature range of $10 \text{ meV} < k_B T < 70 \text{ meV}$. The arch-shaped transmission coefficient curve pro-

vides insights into the potential mechanism underlying the thermoelectric properties of *GeTe* materials with multiple valley degeneracies.

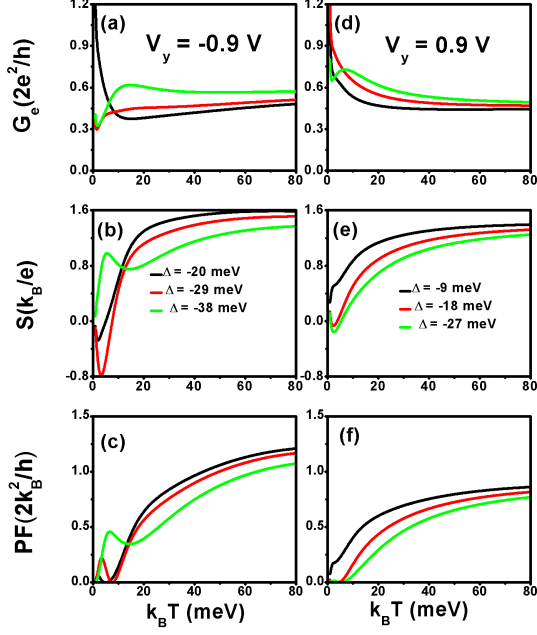


FIG. 9: (a) Electrical conductance (G_e), (b) Seebeck coefficient (S), and (c) power factor ($PF = S^2 G_e$) as functions of temperature for various chemical potential values at $V_y = -0.9$ V. (d) Electrical conductance (G_e), (e) Seebeck coefficient (S), and (f) power factor ($PF = S^2 G_e$) as functions of temperature for various chemical potential values at $V_y = 0.9$ V. The analysis is based on a 4-AB/4-C/4-AB ZGNR segment with $N_z = 81$ (9.84 nm) and $\Gamma_t = 2.7$ eV.

IV. CONCLUSION

We conducted theoretical studies on the electronic and thermoelectric properties of ZGNRs with staggered sublattice potentials described by w-AB/n-C/w-AB using the tight-binding model and Green's function technique. The electronic structures of w-AB/n-C/w-AB ZGNRs exhibit semiconducting phases with valley degeneracy, resulting from band inversion of the flat bands observed in metallic ZGNRs. This valley degeneracy is induced by breaking inversion symmetry in the transverse direction, which can be realized in ZGNRs stacked on separate silicon carbide or hexagonal boron nitride sheets. The electronic structures with valley degeneracy are further modulated by transverse electric fields.

In 4-AB/4-C/4-AB ZGNR segments, the $|\Psi_{\ell,j}(E)|^2$ of level degeneracy are delocalized and asymmetrically

distributed along the transverse direction. Their transmission coefficient ($\mathcal{T}_{LR}(\varepsilon)$) spectra are significantly influenced by contact properties associated with electrode materials. The shape of the $\mathcal{T}_{LR}(\varepsilon)$ curve can be manipulated not only by the magnitude but also by the direction of the applied transverse electric field, characteristics crucial for applications in managing electron heat currents [84–86].

The thermoelectric efficiency of 4-AB/4-C/4-AB ZGNRs with optimized electrical power output favors thermionic-assisted transport (TAT). Level degeneracy enhances electrical conductance while maintaining Seebeck coefficients, thereby enhancing the power factor. In TAT, ZT can also be improved due to the enhanced power factor under conditions where $\kappa_{ph} \gg \kappa_e$. Conversely, in direct ballistic transport (DBT), the power factor is reduced due to the small Seebeck coefficient at low temperatures. As μ approaches and falls below ε_{HO} , significant enhancements in the Seebeck coefficient at high temperatures and modest reductions in electrical conductance lead to enhanced power factors. This phenomenon results from increased electron-hole asymmetrical range with rising temperature in 4-AB/4-C/4-AB ZGNRs. The results in Fig. 9(a), 9(b), and 9(c) within the range of $k_B T = 20$ meV to $k_B T = 70$ meV provide valuable insights into the thermoelectric properties observed in materials like Germanium Telluride [36].

Acknowledgments

This work was supported by the National Science and Technology Council, Taiwan under Contract No. MOST 107-2112-M-008-023MY2.

E-mail address: mtkuo@ee.ncu.edu.tw

Appendix A: Electronic Band Structures of ZGNRs with w-AB/n-C/w-AB Scenario

To further understand the electronic properties depicted in Fig. 2(a), we present the electronic structures of 4-AB/4-C/4-AB for various δ values in Fig. A.1. In Fig. A.1(a) with $\delta = 0$, the electronic structure of 4-AB/4-C/4-AB exhibits metallic properties of ZGNRs, characterized by flat bands near the CNP [66–67]. In Fig. A.1(b), with $\delta = 0.45$ eV, only the frontier conduction and valence subbands are perturbed. Other subbands remain largely unaffected, and a small gap separates the conduction subband from the valence subband due to the presence of staggered sublattice potential. Additionally, the originally flat band observed at $\delta = 0$ is slightly distorted.

Fig. A.1(c) shows the scenario with $\delta = 0.9$ eV, where the frontier conduction and valence subbands exhibit clear valley structures, albeit shallow ones. Tuning δ further from $\delta = 1.35$ eV to $\delta = 2.25$ eV leads to a

significant band inversion in the frontier conduction and valence subbands of ZGNRs. This band inversion mechanism shown in Fig. A.1 does not involve spin-orbit coupling, which is a mechanism often cited for band inversion in materials such as *BiTe* thermoelectrics.

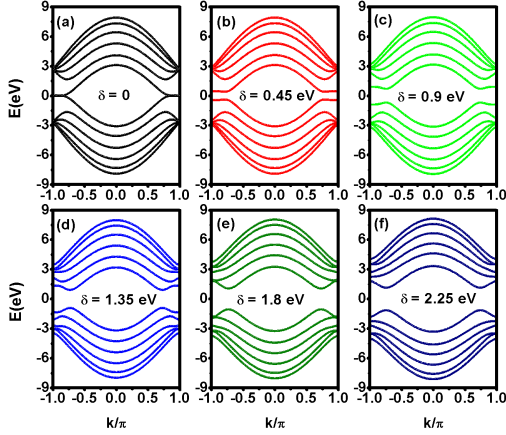


FIG. A.1: Electronic structures of 4-AB/4-C/4-AB ZGNRs for various δ values.

Next, we present the calculated electronic structures of 4-AB/ n -C/4-AB with a fixed $\delta = 0.9$ eV for different values of n in Fig. A.2. As the value of n increases, the band gaps of ZGNRs decrease. While deeper valley structures are enhanced with increasing n , the smaller band gap

tends to suppress the Seebeck coefficient at high temperatures. Additionally, wider ZGNRs can increase phonon thermal conductance. This study focuses specifically on the case of 4-AB/4-C/4-AB ZGNRs.

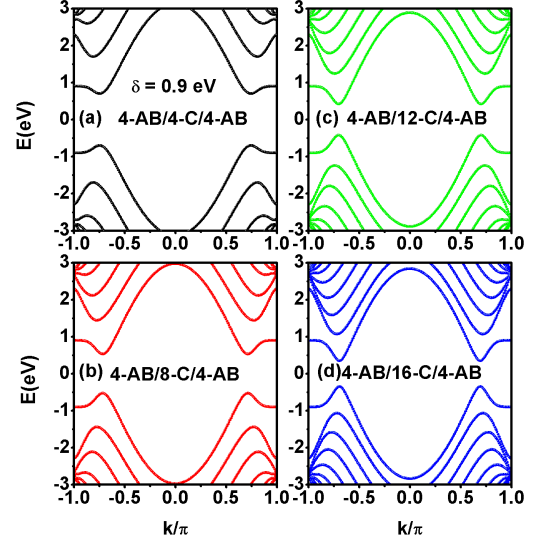


FIG. A.2: Electronic structures of 4-AB/ n -C/4-AB ZGNRs with $\delta = 0.9$ eV for various n values.

- ¹ G.D. Mahan and J. O. Sofo, The best thermoelectric. Proc. Natl. Acad. Sci. USA **93**, 7436 (1996).
- ² G. D. Mahan, B. Sales, and J. Sharp, Thermoelectric materials: New approaches to an old problem, Phys. Today **50**, 42 (1997).
- ³ G. D. Mahan, and L. M. Woods, Multilayer thermionic refrigeration. Phys. Rev. Lett. **80**, 4016 (1998).
- ⁴ G. Chen, M. S. Dresselhaus, G. Dresselhaus, J. P. Fleurial, and T. Caillat, Recent developments in thermoelectric materials, Int. Mater. Rev. **48**, 45 (2003).
- ⁵ K. F. Hsu, S. Loo, F. Guo, W. Chen, J. S. Dyck, C. Uher, T. Hogan, E. K. Polychroniadis, and M. G. Kanatzidis, Cubic AgPbmSbTe_{2+m}: Bulk thermoelectric materials with high figure of merit, Science **303**, 818 (2004).
- ⁶ A. J. Minnich, M. S. Dresselhaus, Z. F. Ren, and G. Chen, Bulk nanostructured thermoelectric materials: current research and future prospects, Energy Environ. Sci. **2**, 466 (2009).
- ⁷ R. Venkatasubramanian, E. Siivola, T. Colpitts, and B. O'Quinn, Thin-film thermoelectric devices with high room-temperature figures of merit, Nature **413**, 597 (2001).
- ⁸ A. I. Boukai, Y. Bunimovich, J. Tahir-Kheli, J. K. Yu, W. A. Goddard III, and J. R. Heath, Silicon nanowires as efficient thermoelectric materials, Nature **451**, 168 (2008).
- ⁹ G. Q. Zhang, B. Kirk, L. A. Jauregui, H. R. Yang, X. F. Xu, Y. P. Chen, and Y. Wu, Rational Synthesis of Ultrathin n-Type Bi₂Te₃ Nanowires with Enhanced Thermoelectric Properties, Nano Lett **12**, 56 (2012).
- ¹⁰ Y. Tian, M. R. Sakr, J. M. Kinder, D. Liang, M. J. MacDonald, R. L. J. Qiu, H. J. Gao, and X. P. A Gao, One-Dimensional Quantum Confinement Effect Modulated Thermoelectric Properties in InAs Nanowires, Nano Lett **12**, 6492 (2012).
- ¹¹ T. C. Harman, P. J. Taylor, M. P. Walsh, and B. E. LaForge, Quantum dot superlattice thermoelectric materials and devices, Science **297**, 2229 (2002).
- ¹² A. Majumdar, Thermoelectricity in semiconductor nanostructures, Science **303**, 777 (2004).
- ¹³ Y. M. Lin and M. S. Dresselhaus, Thermoelectric properties of superlattice nanowires, Phys. Rev. B **68**, 075304 (2003).
- ¹⁴ L.D. Hicks, and M.S Dresselhaus, Thermoelectric figure of merit of a one-dimensional conductor. Phys. Rev. B **47**, 16631 (1993).
- ¹⁵ Y. J. Ouyang and J. Guo, A theoretical study on thermoelectric properties of graphene nanoribbons, Appl. Phys. Lett. **94**, 263107 (2009).
- ¹⁶ H. Sevincli, and G. Cuniberti, Enhanced thermoelectric figure of merit in edge-disordered zigzag graphene nanoribbons, Phys. Rev. B **81**, 113401 (2010).

- ¹⁷ F. Mazzamuto, V. H. Nguyen, Y. Apertet, C. Caer, C. Chassat, J. Saint-Martin, and P. Dollfus, Enhanced thermoelectric properties in graphene nanoribbons by resonant tunneling of electrons, *Phys. Rev. B*, **83**, 235426 (2011).
- ¹⁸ Y. Xu, Z. Y. Li, and W. H. Duan, Thermal and Thermoelectric Properties of Graphene, *Small*, **10**, 2182 (2014).
- ¹⁹ L. Pan, H. J. Liu, X. J. Tan, H. Y. Lv, J. Shi, X. F. Tang, and G. Zheng, Thermoelectric properties of armchair and zigzag silicene nanoribbons, *Chem. Phys. Phys. Chem.* **14**, 13588 (2012).
- ²⁰ K. K. Yang, Y. P. Chen, R. D'Agosta, Y. E. Xie, J. X. Zhong, and A. Rubio, Enhanced thermoelectric properties in hybrid graphene/boron nitride nanoribbons, *Phys. Rev. B* **86**, 045425 (2012).
- ²¹ K. Zburecki, M. Wierzbicki, J. Barnas and R. Swirkowicz, Thermoelectric effects in silicene nanoribbons, *Phys. Rev. B* **88**, 115405 (2013).
- ²² Y. Xu, Z. X. Gan and S. C. Zhang, Enhanced Thermoelectric Performance and Anomalous Seebeck Effects in Topological Insulators, *Phys. Rev. Lett.* **112**, 226801 (2014).
- ²³ P. H. Chang, M. S. Bahramy, N. Nagaosa and B. K. Nikolic, Giant Thermoelectric Effect in Graphene-Based Topological Insulators with Heavy Adatoms and Nanopores, *Nano Lett.*, **14**, 3779 (2014).
- ²⁴ K. S. Novoselov, A. K. Geim, S. V. Morozov, D. Jiang, Y. Zhang, S. V. Dubonos, I. V. Grigorieva and A. A. Firsov, Electric field effect in atomically thin carbon films, *Science*, **306**, 666 (2004).
- ²⁵ H. M. Wang, H. S. Wang, C. X. Ma, L. X. Chen, C. X. Jiang, C. Chen, X. M. Xie, A. P. Li and X. R. Wang, Graphene nanoribbons for quantum electronics, *Nat. Rev. Phys.* **3**, 791 (2021).
- ²⁶ C. H. Tian, W. J. Miao, L. Zhao, and J. G. Wang, Graphene nanoribbons: Current status and challenges as quasi-one-dimensional nanomaterials, *Review in Physics*, **10**, 100082 (2023).
- ²⁷ R. S. Whitney, Most Efficient Quantum Thermoelectric at Finite Power Output, *Phys. Rev. Lett.* **112**, 130601 (2014).
- ²⁸ David. M. T. Kuo and Y. C. Chang, Thermoelectric and thermal rectification properties of quantum dot junctions. *Phys. Rev. B* **81**, 205321 (2010).
- ²⁹ David M. T. Kuo, C. C. Chen, and Y. C. Chang, Large enhancement in thermoelectric efficiency of quantum dot junctions due to increase of level degeneracy, *Phys. Rev. B* **95**, 075432 (2017).
- ³⁰ David. M. T. Kuo and Y. C. Chang, Contact Effects on Thermoelectric Properties of Textured Graphene Nanoribbons, *Nanomaterials*, **12**, 3357 (2022).
- ³¹ David. M. T. Kuo, Thermoelectric properties of armchair graphene nanoribbons with array characteristics, *RSC Advances* **14**, 3517 (2024).
- ³² M. Y. Toriyama, M. K. Brod, L. C. Gomes, F. A. Bipasha, B. A. Assaf, E. Ertekin and G. J. Snyder, Tuning valley degeneracy with band inversion, *J. Mater. Chem. A* **10**, 1588 (2022).
- ³³ Y. L. Jiang et al, Evolution of defect structures leading to high *ZT* in GeTe-based thermoelectric materials, *Nature Communications*, **13**, 6087 (2022).
- ³⁴ B. B. Jiang et al, High figure of merit and power generation in high-entropy GeTe thermoelectrics. *Science* **377**, 208 (2022).
- ³⁵ L. C. Yin et al, Interstitial Cu: An Effective Strategy for High Carrier Mobility and High Thermoelectric Performance in GeTe, *Adv. Funct. Mater.* **33**, 2301750 (2023).
- ³⁶ V. K. Ranganayakulu et al, Ultrahigh *zT* from strong electron-phonon interactions and a low-dimensional Fermi surface, *Energy Environ Sci*, **17**, 1904 (2024).
- ³⁷ J. Cai, P. Ruffieux, R. Jaafar, M. Bieri, T. Braun, S. Blankenburg, M. Muoth, A. P. Seitsonen, M. Saleh, X. Feng, K. Mullen and R. Fasel, Atomically precise bottom-up fabrication of graphene nanoribbons, *Nature*, **466**, 470 (2010).
- ³⁸ J. Z. Liu, B. W. Li, Y. Z. Tan, A. Giannakopoulos, C. Sanchez-Sanchez, D. Beljonne, P. Ruffieux, R. Fasel, X. L. Feng and K. Mullen, Toward Cove-Edged Low Band Gap Graphene Nanoribbons, *J. Am. Chem. Soc.*, **137**, 6097 (2015).
- ³⁹ L. Y. Lee, F. Z. Zhao, T. Cao, I. Jisoon and S. G. Louie, Topological Phases in Cove-Edged and Chevron Graphene Nanoribbons: Geometric Structures, *Z(2)* Invariants, and Junction States, *Nano Lett.* **18**, 7274 (2018).
- ⁴⁰ F. M. Arnold, T. J. Liu, A. Kuc, and T. Heine, Structure-Imposed Electronic Topology in Cove-Edged Graphene Nanoribbons, *Phys. Rev. Lett.* **129**, 216401 (2022).
- ⁴¹ X. Wang, J. Ma, W. H. Zheng, S. Osella, N. Arisnabarreta, J. Droste, J. Serra, O. Ivasenko, A. Lucotti, D. Beljonne, M. Bonn, X. Y. Liu, M. R. Hansen, M. Tommasini, S. De. Feyter, J. Z. Liu, H. I. Wang and X. L. Feng, Cove-Edged Graphene Nanoribbons with Incorporation of Periodic Zigzag-Edge Segments, *J. Am. Chem. Soc.* **144**, 228 (2022).
- ⁴² Y. C. Chen, T. Cao, C. Chen, Z. Pedramraz, D. Haberer, D. G. de Oteyza, R. Fischer, S. G. Louie and M. F. Crommie, Molecular bandgap engineering of bottom-up synthesized graphene nanoribbon heterojunctions, *Nat. Nanotechnol.* **10**, 156 (2015).
- ⁴³ D. J. Rizzo, G. Veber, J. W. Jiang, R. McCurdy, T. Bronner, T. Cao, T. Chen, S. G. Louie, F. R. Fischer and M. F. Crommie, Inducing metallicity in graphene nanoribbons via zero-mode superlattices, *Science* **369**, 1597 (2020).
- ⁴⁴ Q. Sun, Y. Yan, X. L. Yao, K. Mullen, A. Narita, R. Fasel and P. Ruffieux, Evolution of the Topological Energy Band in Graphene Nanoribbons, *J. Phys. Chem. Lett.* **12**, 8679 (2021).
- ⁴⁵ D. J. Rizzo, J. W. Jiang, D. Joshi, G. Veber, C. Bronner, R. A. Durr, P. H. Jacobse, T. Cao, A. Kalayjian, H. Rodriguez, P. Butler, T. Chen, S. G. Louie, F. R. Fischer and M. F. Crommie, Rationally Designed Topological Quantum Dots in Bottom-Up Graphene Nanoribbons, *ACS Nano* **15**, 20633 (2021).
- ⁴⁶ Z. Liu, L. L. Ma, G. Shi, W. Zhou, Y. J. Gong, S. D. Lei, X. B. Yang, J. N. Zhang, J. J. Yu, K. P. Hackenberg, A. Babakhani, J. C. Idrobo, R. Vajtai, J. Lou, and P. M. Ajayan, In-plane heterostructures of graphene and hexagonal boron nitride with controlled domain sizes, *Nat. Nanotechnol.* **8**, 119 (2013).
- ⁴⁷ L. X. Chen, L. He, H. S. Wang, H. M. Wang, S. J. Tang, C. X. Cong, H. Xie, L. Li, H. Xia, and T. X. Li, Oriented graphene nanoribbons embedded in hexagonal boron nitride trenches, *Nat. Commun.* **8**, 14703 (2017).
- ⁴⁸ H. S. Wang et al, Towards chirality control of graphene nanoribbons embedded in hexagonal boron nitride, *Nat. Mater.* **20**, 202 (2021).
- ⁴⁹ J. Bradford, T. S. Cheng, T. S. S. James, A. N. Khlobystov, C. J. Mellor, K. Watanabe, T. Taniguchi, S. V. Novikov, and P. H. Beton, Graphene nanoribbons with hBN passivated edges grown by high-temperature molecular beam epitaxy, *2D Mater.* **10**, 035035 (2023).

- ⁵⁰ G. S. Seal and J. Guo, Bandgap opening in boron nitride confined armchair graphene nanoribbon, *Appl. Phys. Lett.* **98**, 143107 (2011).
- ⁵¹ Y. Ding, Y. Wang and J. Ni, Electronic properties of graphene nanoribbons embedded in boron nitride sheets, *Phys. Rev. B* **95**, 123105 (2009).
- ⁵² G. Lee and K. Cho, Electronic structures of zigzag graphene nanoribbons with edge hydrogenation and oxidation, *Phys. Rev. B* **79**, 165440 (2009).
- ⁵³ J. He, K. Q. Chen, Z. Q. Fan, L. M. Tang and W. P. Hu, Transition from insulator to metal induced by hybridized connection of graphene and boron nitride nanoribbons, *Appl. Phys. Lett.* **97**, 193305 (2010).
- ⁵⁴ J. M. Pruneda, Origin of half-semimetallicity induced at interfaces of C-BN heterostructures, *Phys. Rev. B* **81**, 161409(R) (2010).
- ⁵⁵ J. Jung, Z. H. Qiao, Q. Niu, and A. H. MacDonald, Transport Properties of Graphene Nanoroads in Boron Nitride Sheets, *Nano Lett.* **12**, 2936 (2012).
- ⁵⁶ J. Zhao, P. Ji, Y. Q. Li, R. Li, K. M. Zhang, H. Tian, K. C. Yu, B. Bian, L. H. Hao, X. Xiao, W. Griffin, N. Dudeck, R. Morol, Lei Mal, and W. A. de Heer, Ultra-high mobility semiconducting epitaxial graphene on silicon carbide, *Nature* **625**, 60 (2024).
- ⁵⁷ Z. H. Qiao, S. Y. A. Yang, B. Wang, Y. Q. Yao, and Q. Niu, Spin-polarized and valley helical edge modes in graphene nanoribbons, *Phys. Rev. B* **84**, 035431 (2011).
- ⁵⁸ C. P. Lu, Guohong Li, K. Watanabe, T. Taniguchi, and Eva Y. Andreil, MoS₂: Choice Substrate for Accessing and Tuning the Electronic Properties of Graphene, *Phys. Rev. Lett.* **113**, 156804 (2014).
- ⁵⁹ Q. F. Sun and X. C. Xie, CT-Invariant Quantum Spin Hall Effect in Ferromagnetic Graphene, *Phys. Rev. Lett.* **104**, 066805 (2010).
- ⁶⁰ D. A. Areshkin, D. Gunlycke, and C. T. White, Ballistic transport in graphene nanostrips in the presence of disorder: Importance of edge effects. *Nano Lett.* **7**, 204 (2007).
- ⁶¹ T. B. Martins, A. J. R. da Silva, R. H. Miwa and A. Fazzio, sigma- and pi-defects at graphene nanoribbon edges: Building spin filters. *Nano Lett.* **8**, 2293 (2008).
- ⁶² T. C. Li and S. P. Lu, Quantum conductance of graphene nanoribbons with edge defects, *Phys. Rev. B* **77**, 085408 (2008).
- ⁶³ P. Darancet, V. Olevano and D. Mayou, Coherent electronic transport through graphene constrictions: Subwavelength regime and optical analogy. *Phys. Rev. Lett.* **102**, 136803 (2009).
- ⁶⁴ Y. Matsuda, W. Q. Deng and III W A Goddard, Contact Resistance for "End-Contacted" Metal-Graphene and Metal-Nanotube Interfaces from Quantum Mechanics, *J. Phys. Chem. C* **114**, 17845 (2010).
- ⁶⁵ R. S. Chen, G. L. Ding, Y. Zhou, and S. T. Han, Fermi-level depinning of 2D transition metal dichalcogenide transistors. *J. Mater. Chem. C* **9**, 11407 (2021).
- ⁶⁶ K. Nakada, M. Fujita, G. Dresselhaus and M. S. Dresselhaus, Edge state in graphene ribbons: Nanometer size effect and edge shape dependence, *Phys. Rev. B* **54**, 17954 (1996).
- ⁶⁷ K. Wakabayashi, M. Fujita, H. Ajiki and M. Sigrist, Electronic and magnetic properties of nanographite ribbons, *Phys. Rev. B* **59**, 8271 (1999).
- ⁶⁸ M. Y. Toriyama and G. Jeffrey Snyder, Are topological insulators promising thermoelectrics, *Mater. Horiz.* **11**, 1188 (2024).
- ⁶⁹ M. Y. Toriyama and G. Jeffrey Snyder, Band inversion-driven warping and high valley degeneracy, *Cell Reports Physical Science* **4**, 101392 (2023).
- ⁷⁰ Z. Y. Zhu, Y. C. Cheng, and Udo Schwingenschlogl, Band inversion mechanism in topological insulators: A guideline for materials design, *Phys. Rev. B* **85**, 235401 (2012).
- ⁷¹ F. Z. Zhao, T. Cao, and S. G. Louie, Topological Phases in Graphene Nanoribbons Tuned by Electric Fields, *Phys. Rev. Lett.* **127**, 166401 (2021).
- ⁷² J. R. Schaibley, H. Y. Yu, G. Clark, P. Rivera, J. S. Ross, K. L. Seyler, W. Yao, and X. D. Xu, Valleytronics in 2D materials, *Nat. Rev. Materials.* **1**, 16055 (2016).
- ⁷³ A. Rycerz, J. Tworzydło, C. W. J. Beenakker, Valley filter and valley valve in graphene, *Nat. Phys.* **3**, 172 (2007).
- ⁷⁴ C. Mai, A. Barrette, Y. F. Yu, Y. G. Semenov, K. W. Kim, L. Y. Cao, and K. Gundogdu, Many-Body Effects in Valleytronics: Direct Measurement of Valley Lifetimes in Single-Layer MoS₂, *Nano Lett.* **14**, 202 (2014).
- ⁷⁵ M. Ezawa, Spin valleytronics in silicene: Quantum spin Hall-quantum anomalous Hall insulators and single-valley semimetals, *Phys. Rev. B* **87**, 155415 (2013).
- ⁷⁶ J. P. Llinas, A. Fairbrother, G. Borin Barin, W. Shi, K. Lee, S. Wu, B. Y. Choi, R. Braganza, J. Lear, N. Kau et al., Short-channel field-effect transistors with 9-atom and 13-atom wide graphene nanoribbons. *Nat. Commun.* **8**, 633 (2017).
- ⁷⁷ P. H. Jacobse, A. Kimouche, T. Gebraad, M. M. Ervasti, J. M. Thijssen, P. Liljeroth, and I. Swart, Electronic components embedded in a single graphene nanoribbon. *Nat Commun.* **8**, 119 (2017).
- ⁷⁸ K. W. Lee and C. E. Lee, Transverse electric field-induced quantum valley Hall effects in zigzag-edge graphene nanoribbons, *Phys. Lett. A* **382**, 2137 (2018).
- ⁷⁹ Y. T. Zhang, Q. F. Sun and X. C. Xie, The effect of disorder on the valley-dependent transport in zigzag graphene nanoribbons, *J. Appl. Phys.* **109**, 123718 (2011).
- ⁸⁰ H. Zheng, H. J. Liu, X. J. Ta, H. Y. Lv, L. Pan, J. Shi, and X. F. Tang, Enhanced thermoelectric performance of graphene nanoribbons. *Appl. Phys. Lett.* **100**, 093104 (2012).
- ⁸¹ V. T. Tran, J. S. Martin and P. Dollfus, High thermoelectric performance in graphene/BN interface engineering, *Nanotechnology*, **26**, 495202 (2015).
- ⁸² P. Dollfus, V. H. Nguyen and J. Saint-Martin, Thermoelectric effects in graphene nanostructures, *J. Phys.: Condens. Matter* **27** 133204 (2015).
- ⁸³ L. A. Algharagholy, Q. A. Galiby, H. A. Marhoon, Hatef Sadeghi, H. M. Abduljalil and C. J. Lambert, Tuning thermoelectric properties of graphene/boron nitride heterostructures, *Nanotechnology* **26**, 475401 (2015).
- ⁸⁴ M. J. Martinez-Perez, A. Fornieri and F. Giazotto, Rectification of electronic heat current by a hybrid thermal diode, *Nat. Nanotech.* **10**, 303 (2015).
- ⁸⁵ G. T. Craven, D. H. He and A. Nitzan, Electron-Transfer-Induced Thermal and Thermoelectric Rectification, *Phys. Rev. Lett.* **121**, 247704 (2018).
- ⁸⁶ David M. T. Kuo, Thermal rectification through the topological states of asymmetrical length armchair graphene nanoribbons heterostructures with vacancies, *Nanotechnology* **34**, 505401 (2023).